molecules

MDPI

Article

IrO_2 Oxygen Evolution Catalysts Prepared by an Optimized Photodeposition Process on TiO_2 Substrates

Angeliki Banti [1,*], Christina Zafeiridou [1], Michail Charalampakis [2], Olga-Niki Spyridou [1], Jenia Georgieva [3], Vasileios Binas [1,2], Efrosyni Mitrousi [1] and Sotiris Sotiropoulos [1,*]

[1] Physical Chemistry Laboratory, Department of Chemistry, Aristotle University of Thessaloniki, 54124 Thessaloniki, Greece; zafeirid@ualberta.ca (C.Z.); nikiolga9@gmail.com (O.-N.S.); vbinas@chem.auth.gr (V.B.); mitrouse@chem.auth.gr (E.M.)

[2] Institute of Electronic Structure and Laser, Foundation for Research and Technology-Hellas (FORTH-IESL), 70013 Herakleion, Greece; michalisxaral@gmail.com

[3] Rostislaw Kaischew Institute of Physical Chemistry, Bulgarian Academy of Sciences, 1113 Sofia, Bulgaria; jenia@ipc.bas.bg

* Correspondence: ampantic@chem.auth.gr (A.B.); eczss@chem.auth.gr (S.S.)

Abstract: Preparing high-performance oxygen evolution reaction (OER) catalysts with low precious metal loadings for water electrolysis applications (e.g., for green hydrogen production) is challenging and requires electrically conductive, high-surface-area, and stable support materials. Combining the properties of stable TiO_2 with those of active iridium oxide, we synthesized highly active electrodes for OER in acidic media. TiO_2 powders (both commercially available Degussa P-25® and hydrothermally prepared in the laboratory from $TiOSO_4$, either as received/prepared or following ammonolysis to be converted to titania black), were decorated with IrO_2 by UV photodeposition from Ir(III) aqueous solutions of varied methanol scavenger concentrations. TEM, EDS, FESEM, XPS, and XRD measurements demonstrate that the optimized version of the photodeposition preparation method (i.e., with no added methanol) leads to direct deposition of well-dispersed IrO_2 nanoparticles. The electroactive surface area and electrocatalytic performance towards OER of these catalysts have been evaluated by cyclic voltammetry (CV), Linear Sweep Voltammetry (LSV), and Electrochemical Impedance Spectroscopy (EIS) in 0.1 M $HClO_4$ solutions. All TiO_2-based catalysts exhibited better mass-specific (as well as intrinsic) OER activity than commercial unsupported IrO_2, with the best of them (IrO_2 on Degussa P-25® TiO_2 and laboratory-made TiO_2 black) showing 100 $mAmg_{Ir}^{-1}$ at an overpotential of η = 243 mV. Chronoamperometry (CA) experiments also proved good medium-term stability of the optimum IrO_2/TiO_2 electrodes during OER.

Keywords: iridium nanoparticles; titanium oxide; photodeposition; oxygen evolution reaction

check for updates

Citation: Banti, A.; Zafeiridou, C.; Charalampakis, M.; Spyridou, O.-N.; Georgieva, J.; Binas, V.; Mitrousi, E.; Sotiropoulos, S. IrO_2 Oxygen Evolution Catalysts Prepared by an Optimized Photodeposition Process on TiO_2 Substrates. *Molecules* **2024**, *29*, 2392. https://doi.org/10.3390/molecules29102392

Academic Editor: Emmanuel Koudoumas

Received: 14 April 2024
Revised: 5 May 2024
Accepted: 16 May 2024
Published: 19 May 2024

Copyright: © 2024 by the authors. Licensee MDPI, Basel, Switzerland. This article is an open access article distributed under the terms and conditions of the Creative Commons Attribution (CC BY) license (https://creativecommons.org/licenses/by/4.0/).

1. Introduction

Among water splitting technologies (towards a hydrogen economy [1]), proton exchange membrane water electrolyzers (PEMWEs), especially when coupled with renewable energy sources, have been considered as the most promising and appealing systems for high-purity hydrogen production due to their fast load change, high current density, and energy efficiency [2]. However, the highly corrosive operating potential (E > 1.5 V vs. RHE), the sluggish kinetics of the OER, and the acidic environment (pH < 1) at the anode of a PEMWE cell are the main hindrances for the water electrolysis reaction, and studies have focused on investigating suitable stable and low-overpotential OER catalysts [3]. Among the electrode materials quoted in the literature, and in line with the relevant catalytic activity volcano plots as well as stability issues, only precious metal oxides, especially IrO_2 and iridium-based oxides, are suitable anode catalysts, as these combine high catalytic activity and long-term stability in the acidic conditions of PEMWEs [4]. Considering the high cost and limited availability of iridium, many efforts have been devoted to preparing

a cost-effective OER electrocatalyst with the minimum amount of the noble and scarce metal. This can be achieved by increasing the intrinsic catalytic activity of IrO_2 as well as its surface area; both challenges can be addressed by the choice of an appropriate catalyst support material [5].

Among various support candidates, TiO_2 is a promising material both at a pilot scale and for large scale applications, given its low cost, abundance, high stability, corrosion resistance, and mature industry production [6,7]. Despite its poor electrical conductivity and catalytic activity, the decoration of the TiO_2 oxide support with conducting IrO_2 nanoparticles as well as the electronic interaction between them form an electrically percolating structure (with a specific conductivity of >0.1 S cm^{-1}) with improved overall activity and stability [8–12], in line with theoretical predictions [13].

Preparation methods for IrO_x/TiO_2 catalysts include the Adams fusion method [10,12,14,15], thermal treatment in air or H_2 [11,16–18], hydrothermal reactions [19,20], and electrodeposition [21,22]. Photocatalytic deposition of IrO_x on semiconductors is neither a common practice nor a straightforward process from a mechanistic point of view (it usually involves photolytic hydrolysis of Ir salts), among the number of methods reported for IrO_x preparation [23]. There have been very few publications on Ir or IrO_x photodeposition on semiconductor substrates from Ir(III) or Ir(IV) solutions [24–27] and a single one from Ir(III) complexes onto TiO_2 photoanodes [27]. We have recently photodeposited Ir/IrO_x from Ir(III) solutions onto TiO_2 using methanol as a hole scavenger and testing the resulting materials as a catalyst for OER in the dark [28]. However, the role of methanol and the mechanism of photodeposition remained unclear; commercial Degussa P25® was the only substrate used and the resulting catalyst did not outperform the commercial IrO_2 catalyst for OER.

The aim of the work presented here has been to decipher the mechanism of IrO_x photodeposition onto TiO_2, explore the use of various TiO_2 substrates, and optimize the OER performance of the thus prepared IrO_x/TiO_2 material. To that direction, (a) we have studied the effect of methanol on Ir deposition; (b) we have used four different TiO_2 supports: Degussa P25® TiO_2, laboratory-made TiO_2 from titanium oxysulphate, and their titania black analogs prepared by ammonolysis (seeking alternative, more conducting substrates); and (c) we have tested the materials' catalytic performance towards OER by CV, LSV, EIS, and CA electrochemical techniques. Hence, the main novelty of this work is unraveling the mechanism of Ir/IrO_x photodeposition on TiO_2 and preparing catalysts that can outperform the state-of-the-art Ir-based OER catalysts, in terms of Ir mass-specific activity.

2. Results

2.1. Structural, Chemical, and Morphological Characterization of TiO_2 Materials

XRD patterns were recorded for commercial Degussa P25® TiO_2 ("white-P25" hereafter), black TiO_2 P25® produced by ammonolysis (see Section 4 below) ("black-P25" hereafter), laboratory-made TiO_2 from titanium oxysulfate ("white-TiO_2-oxy" hereafter), and black TiO_2-oxysulfate nanoparticles also produced by ammonolysis (see Experimental below) ("black-TiO_2-oxy" hereafter). These are illustrated in Figure 1a,b. Diffraction peaks at 2θ values of 25.3°, 36.9°, 48.1°, 53.9°, 55.1°, and 62.7° can be assigned to (101), (004), (200), (105), (211), and (116) planes of the anatase phase. The additional peaks at 27.4°, 36°, 41.2°, 54.3°, 56.6°, and 68.9° can be ascribed to (110), (101), (111), (211), (220), and (301) planes of the rutile phase. TiO_2 P25® nanoparticles consist of a mixture of anatase and rutile phases as expected for the much-studied commercial material. In contrast, for the laboratory-prepared TiO_2-oxy catalysts, the TiO_2 rutile phase is not present. The intensity of all these peaks before and after ammonolysis is stable, which means that the structure of TiO_2 remains the same in both their "white" and "black" forms. Using the Scherrer equation, the average TiO_2 crystallite size was estimated to be 21.2 and 23.1 nm for white-P25 and black-P25, respectively, and 29.6 nm and 28.5 nm for white-TiO_2-oxy and black-TiO_2-oxy, respectively (i.e., the laboratory-made materials have larger crystallites).

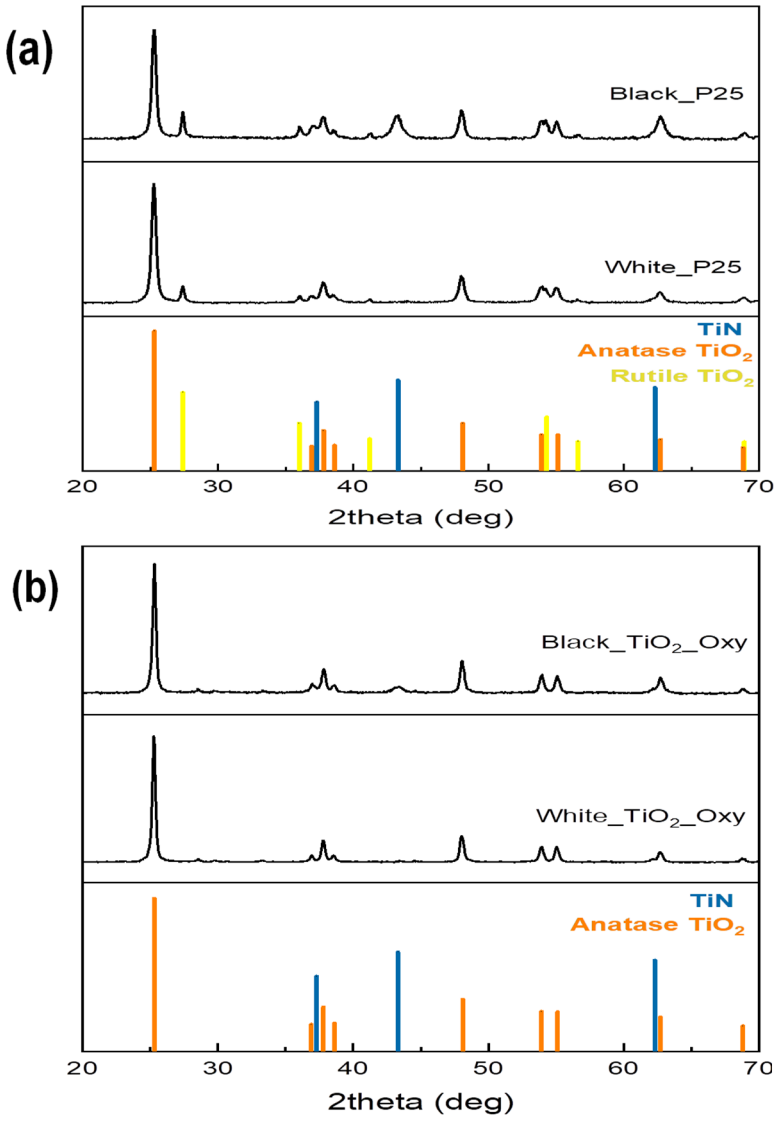

Figure 1. XRD patterns of (**a**) TiO_2 P25® and (**b**) TiO_2-oxy, before ("white") and after ammonolysis ("black"), respectively.

The only significant change in the XRD diffractograms after the ammonolysis process is that both materials show new rutile peaks which correspond to the formation of titanium nitride (TiN); these peaks appear at 2θ values of 37.3°, 43.3°, and 62.3° and they can be indexed to (111), (200) and (220), planes.

The morphology of the TiO_2 powders can be seen in the FESEM images of Figure 2 below. White-P25 (Figure 2a) and black-P25 (Figure 2b) consist of nanoparticles with diameters around ~20 nm and have similar morphology (in black-P25, nanoparticles are slightly more agglomerated). White-TiO_2-oxy (Figure 2c) consists of nanoparticles (~30 nm) that aggregate into rod-like structures which change into smaller nodular particles and rougher aggregates upon their transformation to black-TiO_2-oxy (Figure 2d). The nanoparticle size agrees with calculations from the XRD data, using the Scherrer equation.

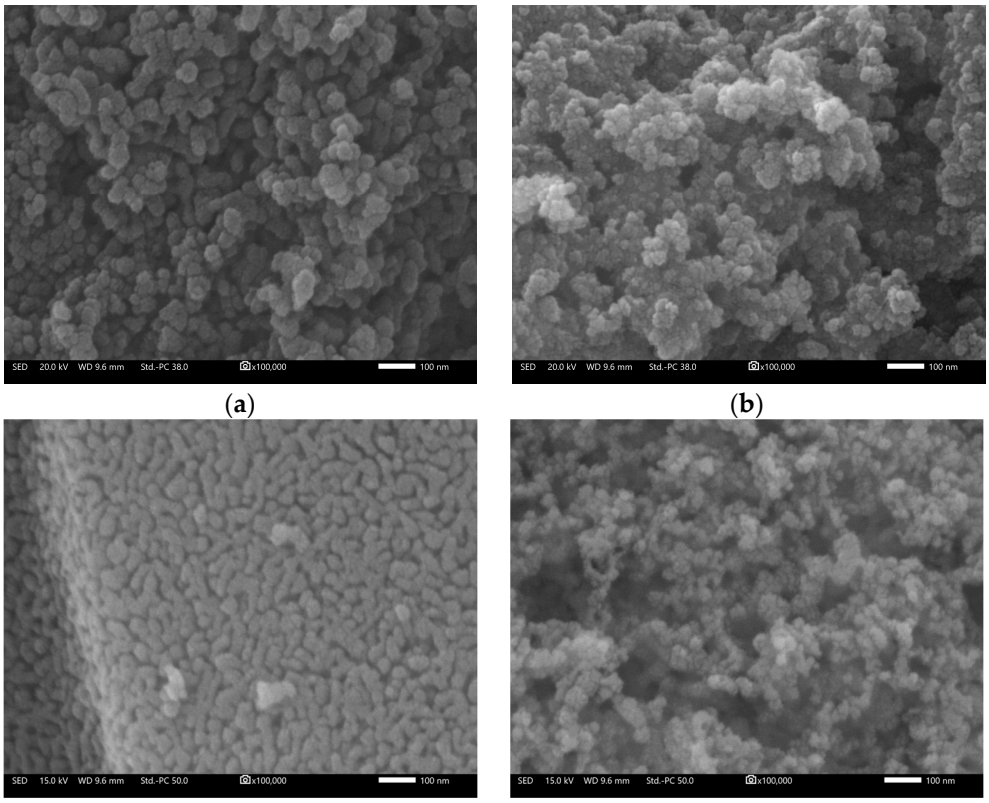

Figure 2. FESEM images of (**a**,**b**) white-P25 and black-P25 and (**c**,**d**) white-TiO_2-oxy and black-TiO_2-oxy (scale bar corresponds to a length of 100 nm).

In addition, elemental analysis (Table 1) and EDS mapping confirms the presence of titanium and oxygen in the appropriate ratios for these oxides as well as the presence of nitrogen in the ammonia-treated samples, due to TiN formation.

Table 1. EDS elemental analysis of the TiO_2 powders before and after ammonolysis.

	Ti (%)	O (%)	C (%)	N (%)
white-P25	25.9	62.7	11.4	-
black-P25	26.8	69.6	-	3.6
white-TiO_2-oxy	28.3	63.9	7.8	-
black-TiO_2-oxy	28.9	68.7	-	2.4

The diffuse reflectance spectra (DRS) of TiO_2 nanoparticles before and after ammonolysis are shown in Figure 3a,b (for P25 and TiO_2-oxy samples, respectively), with the corresponding Tauc plots in Figure 3c,d. The former plots confirm that the "black" catalyst variants absorb light in the visible range too. The optical band gaps of the commercial (P25) and synthesized (TiO_2-oxy) photocatalysts were estimated using the Tauc method, as described in Section 4 below. For white-P25, this can be estimated at 3.06 eV and can be attributed to the mixture of anatase (3.2 eV) and rutile (3.0 eV) phases of TiO_2 (Figure 3c); for white-TiO_2-oxy, it is estimated at 3.21 eV, which agrees with the anatase phase of TiO_2. Although for the "black" variants the Tauc plots cannot lead to accurate band gap values, these can be approximated to $\leq$1 eV for black-P25 and ca 1.5 eV for black-TiO_2-oxy. The significant decrease in the band gap of ammonia-treated samples should also lead to a substantial increase in their electronic conductivity. The maximum absorbance of white-TiO_2 and white-TiO_2-oxy at 365 and 300 nm, respectively, means that UV illumination is mandatory for Ir/IrO_x photodeposition. On the contrary, the absorbance of ammonia-treated

("black") samples means that photodeposition could, in principle, take place under visible light illumination too (however, this has not been possible).

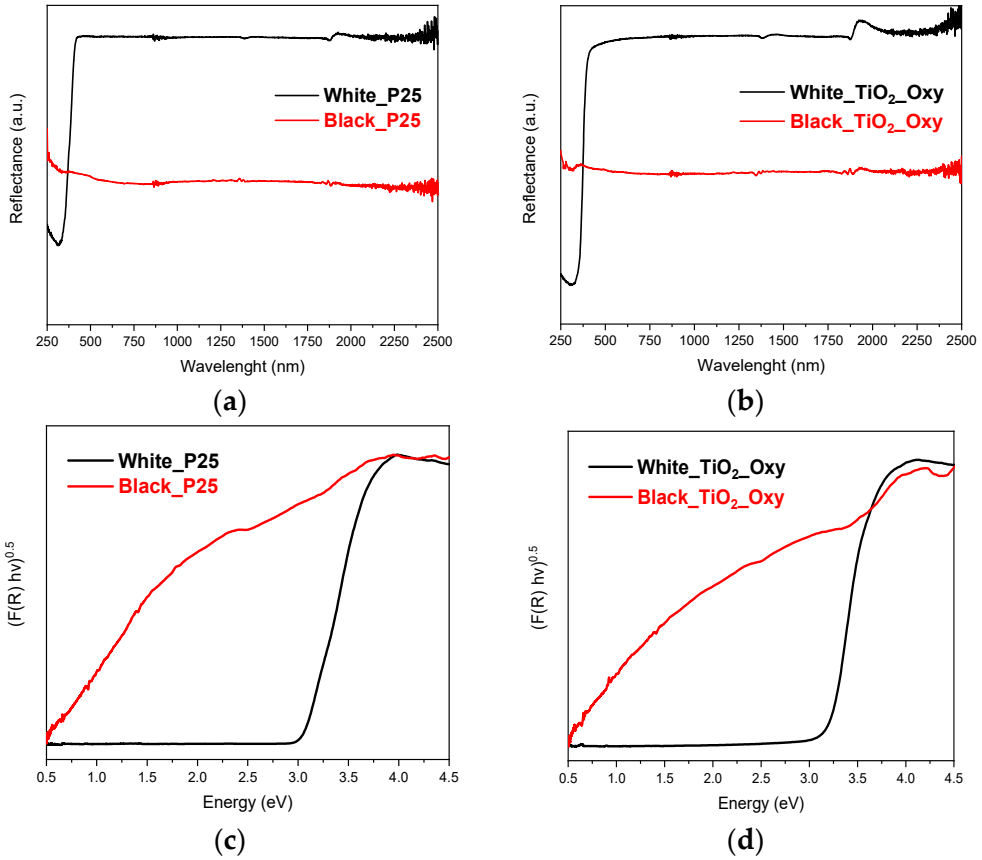

Figure 3. UV-vis diffuse reflectance spectra of TiO_2 nanoparticles ((**a**): P25; (**b**): TiO_2-oxy) and corresponding Tauc plots ((**c**): P25; (**d**): TiO_2-oxy).

2.2. Structural, Chemical, and Morphological Characterization of IrO_x/TiO_2 Materials

The XRD patterns of IrO_x/TiO_2 modified samples did not show well-defined peaks of crystalline IrO_2 and were practically identical to those of Figure 1, pointing to the catalyst being deposited in its amorphous form. (It should be noted that literature data [29,30] indicate that IrO_x catalysts are more active for OER if the material crystallinity is low or intermediate.).

The morphology of the electroactive IrO_x particles is expected to have an important influence on their surface area and on their intrinsic catalytic activity (via their interaction with the substrate) as well as, in this case, on electronic conductivity (since the latter is expected to depend on interparticle contacts). TEM analysis was performed to characterize the morphology of the IrO_2/TiO_2 electrocatalysts.

Figure 4a shows the morphology of the photocatalytically prepared powder of IrO_2/TiO_2 (white-P25®), while Figure 4b depicts that of the commercial IrO_2 catalyst (Alfa Aesar, Karlsruhe, Germany). TEM micrographs provide a first indication of the successful photodeposition of Ir or IrO_2 particles/films (26% *w*/*w* Ir, as further confirmed by EDS) onto the TiO_x particles (the latter having a ca 30 nm nominal size in the case of white-P25®). Ir or IrO_x can be seen as black areas, partly covering the TiO_2 particles, in a non-uniform manner. On the other hand, unsupported commercial IrO_2 nanoparticles (of 2–3 nm nominal size) tend to form aggregates of different sizes.

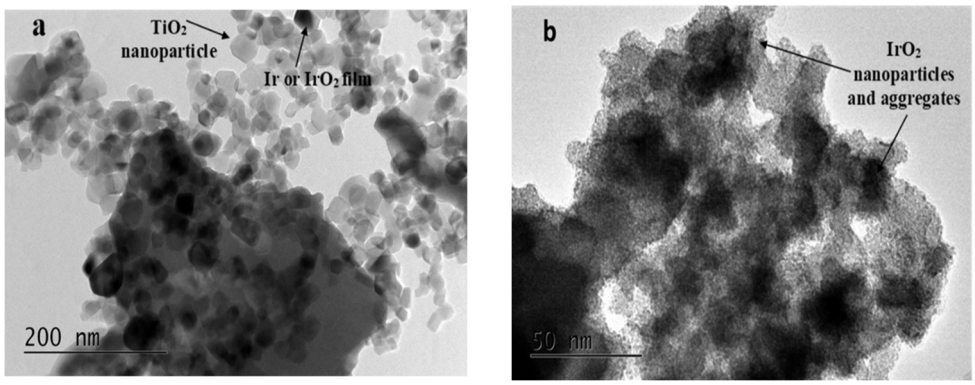

Figure 4. TEM images of (**a**) the photocatalytically prepared powder IrO_2/TiO_2 (white-P25®) and of (**b**) commercial IrO_2 (scale bars correspond to a length of 200 nm (**a**) and 50 nm (**b**)).

Higher-resolution TEM images of all the obtained catalysts are shown in Figure 5a–d and a uniform dispersion of Ir/IrO_x nanoparticles on the larger TiO_2 support particles can be seen. Such a good conducting Ir/IrO_x particle dispersion is crucial for providing good interparticle contact and electronic conductivity. The energy-dispersive spectroscopy (EDS) of the samples shows the existence of Ir—more specifically, for all catalysts, a ca 26 *w*/*w* % Ir content, except for black-P25 with a 15 *w*/*w* % Ir content.

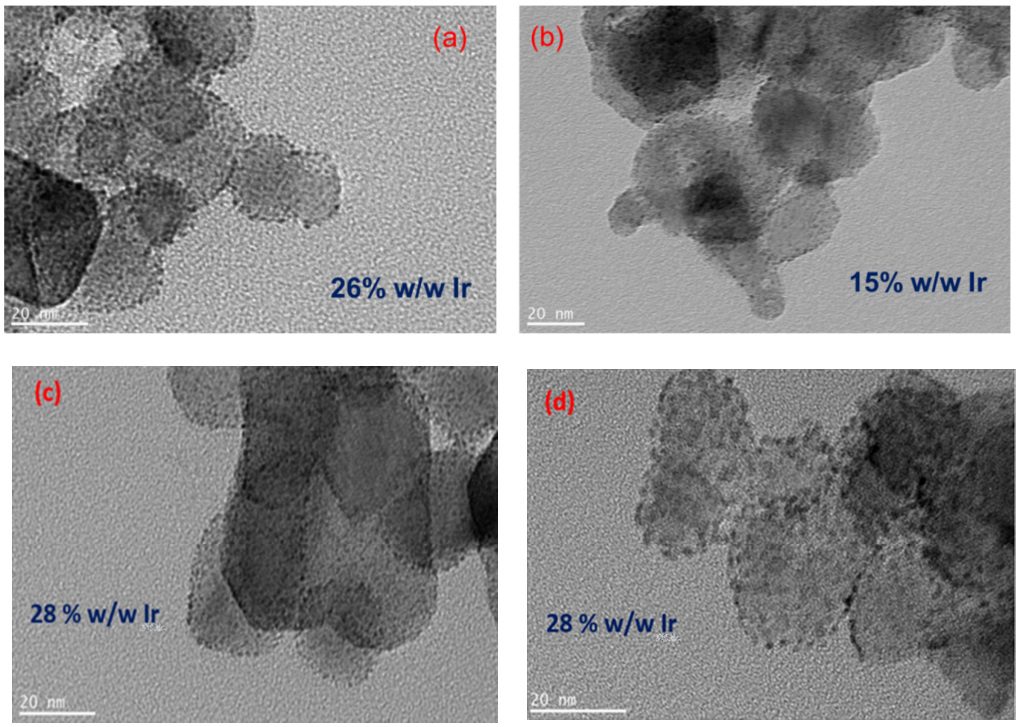

Figure 5. TEM micrographs of (**a**) IrO_x/TiO_2 (white-P25), (**b**) IrO_x/TiO_2 (black-P25), (**c**) IrO_x/TiO_2 (white-TiO_2-oxy) and (**d**) IrO_x/TiO_2 (black-TiO_2-oxy) (scale bar corresponds to a length of 20 nm).

The chemical state of Ir in the TiO_2-supported catalyst was examined by XPS analysis for catalysts prepared in the presence and absence of methanol (Figure 6). The Ir4f peak was used as a first approach for chemical state identification. Measurements at the 4f band of the sample resulted in peak positions of 65.4 eV and 62.4 eV for the Ir 4f5/2 and Ir 4f7/2 peaks, respectively. These values are close to those reported for hydrated amorphous iridium dioxide, which also correlates with the XRD results.

Fitting the data to a curve resulting from the convolution of peaks corresponding to the various oxidation states of Ir proves that the catalyst prepared in pure water (Figure 6a)

consists almost exclusively of iridium oxides (mainly iridium dioxide-Ir(IV)). However, there is some metallic Ir (Ir(0)) when MeOH is added to the preparation solution (Figure 6b) since the anodic deposition route (Ir(III) oxidized by photogenerated holes) may be partially suppressed (as MeOH competes for holes) and the cathodic deposition route (Ir(III) reduced to Ir by photogenerated electrons) may start to operate too (see also Section 3 below).

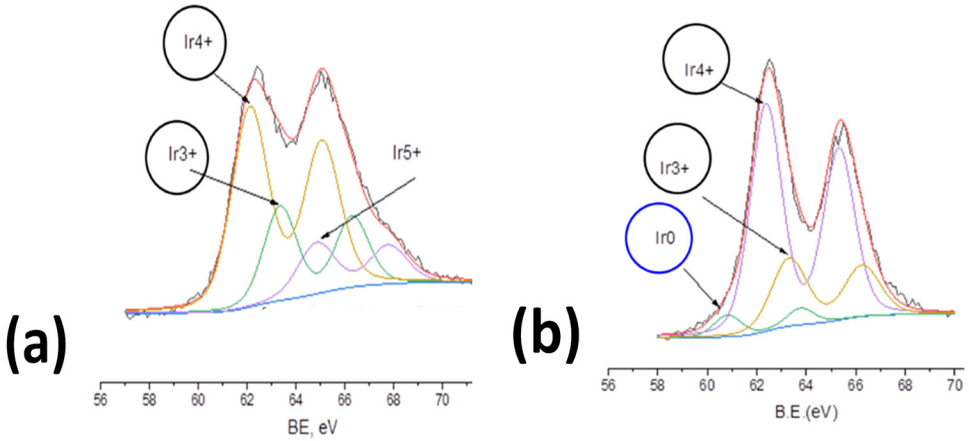

Figure 6. X-ray photoelectron spectra in the Ir4f binding energy range of IrO_x/TiO_2 (white-P25) powder nanocatalyst prepared by UV photodeposition in the absence (**a**) and presence (**b**) of 0.15% *v*/*v* MeOH.

2.3. Electrochemical Performance

IrO_x surface electrochemistry was studied by cyclic voltammetry (CV) experiments in the potential range between hydrogen and oxygen evolution (−0.30 V to +1.10 V vs. SCE) at a 25 mV s^{-1} potential sweep rate. Figure 7 shows the stabilized CV curve for each catalyst (prepared in the absence of methanol). On the anodic part of the CV curve of the commercial, unsupported IrO_x catalyst (Inset to Figure 7), one can clearly observe two peaks corresponding to the transformation of Ir(III) to Ir(IV) and Ir(IV) to Ir(V), typical of IrO_x surface electrochemistry of thermally or electrochemically (by anodization) prepared IrO_x catalysts [29,30]. On the other hand, the photochemically prepared catalysts (main Figure 7) show only one oxidation peak (at ca 0.9 V, corresponding to the Ir(IV) to Ir(V) transformation), pointing to the initial photodeposition mainly of Ir(IV) as IrO_2 on the TiO_2 support, which can only be further oxidized to Ir(V) (see also Discussion below). Also, the electrochemically active surface area of the prepared catalysts is lower than that of the commercial one (for similar Ir loadings in the 0.5–1 mg cm^{-2} range). Given the similar particle morphology of the commercial and prepared IrO_x particles (see Figure 5), this difference may be attributed to the TiO_2 substrate, which cannot provide sufficient electronic conductivity between all IrO_x nanoparticles. Only those IrO_x nanoparticles that are in contact with each other and eventually with the glassy carbon (GC) electrode current collector can act as electroactive material.

Figure 8 depicts the effect of methanol used in catalyst preparation based on surface electrochemistry. An absence of methanol (the purple line) leads to higher iridium content (26 *w*/*w* % as confirmed by EDS) and thus a higher electroactive area and dominance of the Ir(IV) to Ir(V) peak. The suppression of iridium deposition when methanol is added can be inferred by the suppression of Ir surface electrochemistry (and is confirmed by EDS results that give 19% and 2.5% *w*/*w* Ir in the presence of 0.15% and 1.5% *v*/*v* MeOH). This is additional proof that IrO_x is formed by Ir(III) oxidation by photogenerated holes at the TiO_2 valence band where MeOH also competes for these photogenerated holes. (Note also that, in the case of 0.15% *v*/*v* MeOH (green line curve), there appears an oxidation wave at ca. +0.5 V corresponding to the Ir(III) to Ir(IV) transformation, indicative of the presence of some metallic Ir too, which is initially converted to Ir(III).).

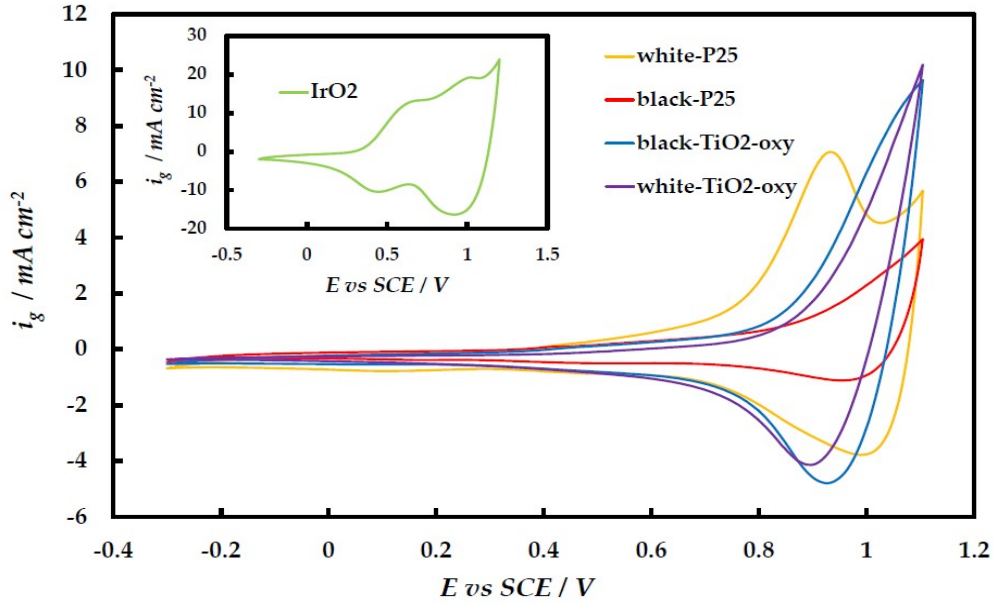

Figure 7. Cyclic voltammetry curves of IrO_x/TiO_2 electrodes as well as of commercial IrO_2 electrode (inset), at 25 mV s^{-1}, in a deaerated 0.1 M $HClO_4$ solution. Current density, i_g, is reported per geometric glassy carbon electrode current collector area.

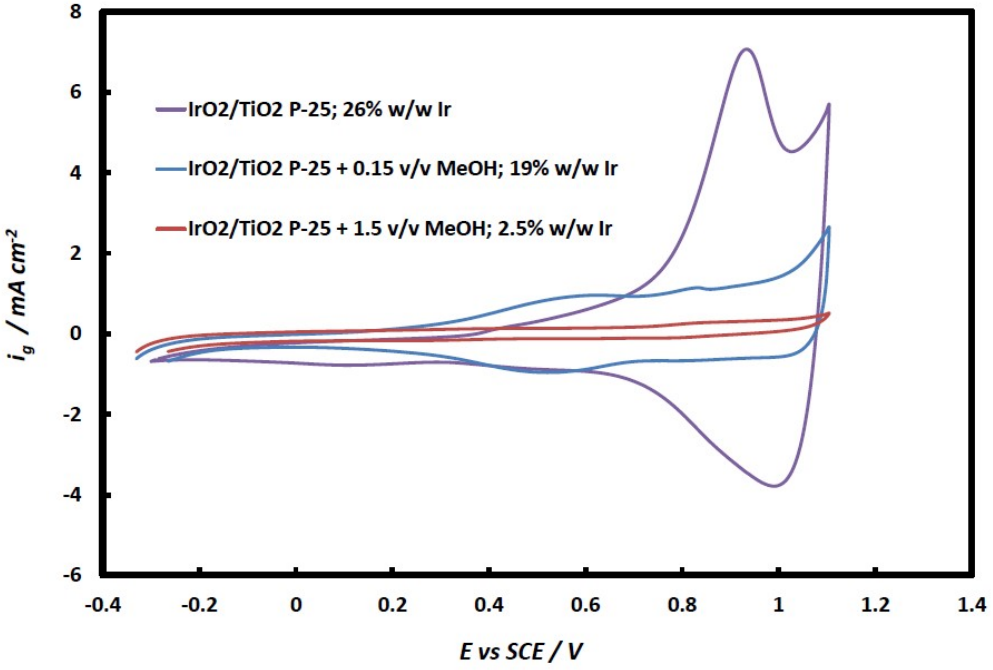

Figure 8. Effect of MeOH content (0, 0.15, 1.5% v/v) during catalyst preparation by photodeposition onto TiO_2 from Ir(III) chloro-complex solutions to Ir/IrO_2 surface electrochemistry.

Near-steady-state Linear Sweep Voltammetry (LSV) at a slow potential sweep rate (5 mV s^{-1}) was employed to investigate the OER activity of the Ir-based catalysts. In Figure 9, currents, i_m, are reported per Ir mass, and all prepared catalysts (except for those supported on black-P25, bearing the lower Ir content and hence lower conductivity) show improved mass activity compared to the commercial IrO_2 catalyst. This means that a higher intrinsic catalytic activity of the prepared catalysts (because of strong IrO_2 and TiO_2–support interactions) offsets their lower electroactive surface area (because of their lower electronic conductivity and catalyst utilization). This is further confirmed by the LSVs of Figure 9, whereby the OER currents are normalized per the charge corresponding

to the 1e$^-$ transformation of Ir species, i.e., per its electroactive surface area, resulting in a current descriptor, i_q, that should be independent of surface area and catalyst utilization (e.g., by conductivity restrictions). The intrinsic catalytic activities of IrO_2 onto white-P25, black-P25, and black-TiO_2-oxy are almost identical and higher than that of IrO_2 on white-TiO_2-oxy and commercial unsupported IrO_2. A mismatch between Ir and Ti size within their oxide network may destabilize Ir-OH bonds (a reactive intermediate of OER) and increase OER activity.

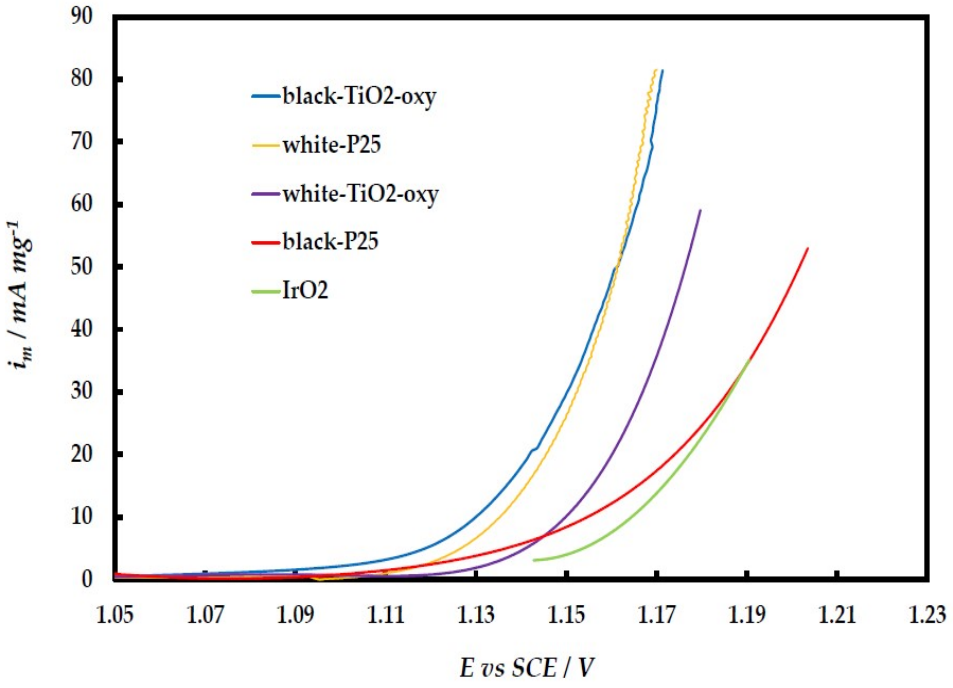

(**a**)

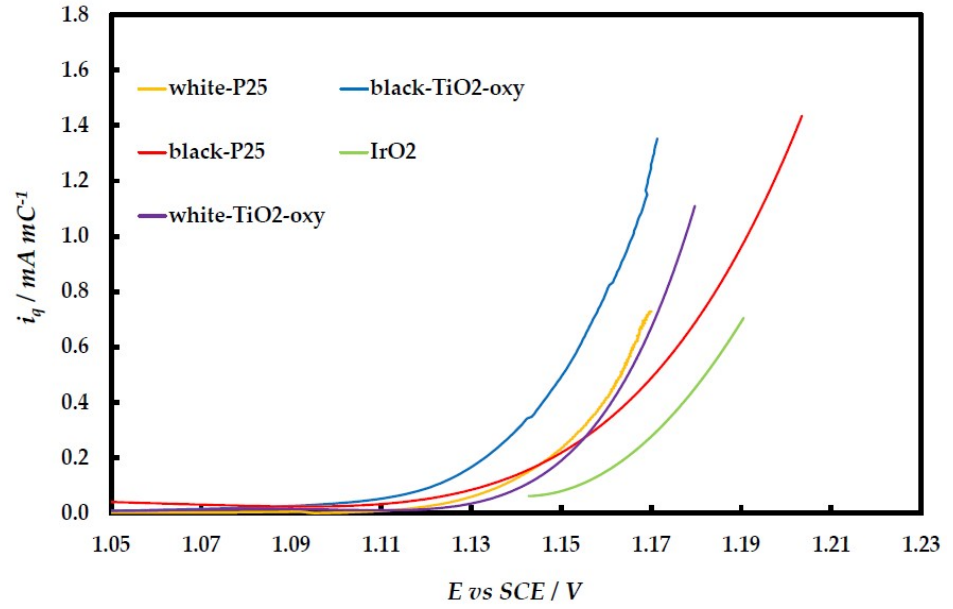

(**b**)

Figure 9. LSVs at 1600 rpm and 5 mVs^{-1} (**a**) per mg of Ir and (**b**) per mC of Ir(IV) to Ir(V) transformation. The potential has been corrected for IR-drop.

Electrochemical Impedance Spectroscopy measurements were performed at 1.2 V in the frequency range of 100 kHz to 100 mHz for the best catalysts according to LSV screening

(of Figure 9 above). The experimental data are presented as Nyquist plots in Figure 10 and were fitted to the equivalent electrical circuit $R_s[R_fQ_f][R_{ct}Q_{dl}]$ (inset of Figure 10). R_s corresponds to the ohmic losses (due to the ionic resistance of the solution between the reference and working electrodes, as well as the electronic resistance of the dispersed IrO_2 electrode); R_fQ_f accounts for the characteristics of ionic transport through the porous electrode and $R_{ct}Q_{dl}$ to the OER charge transfer process and the constant-phase element of the IrO_2/electrolyte interface. (Q_{dl} is transformed to double-layer capacitance C_{dl} using the Mansfield or Brug equations [31,32].) It has recently been argued that low $R_{ct}C_{dl}$ values mean high intrinsic electrocatalytic activity [33].

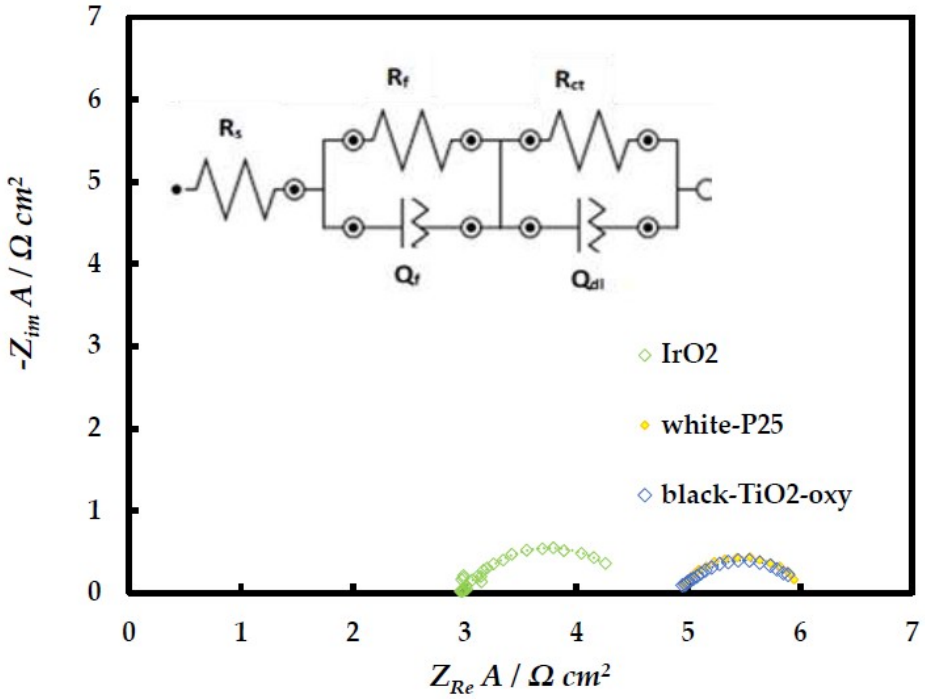

Figure 10. Nyquist plots of IrO_2-based catalysts at 1.2 V.

Table 2 below shows the results of equivalent circuit analysis, from which it follows that the intrinsic catalytic activity of the IrO_2/TiO_2 catalysts towards OER is higher than that of commercial IrO_2, as the former are characterized by lower $R_{ct}C_{dl}$ values.

Table 2. Parameters of the fitted equivalent circuit $[R_s(R_fQ_f)(R_{ct}Q_{dl})]$ to EIS results, for the commercial IrO_2, white-25, and black-TiO_2-oxy electrodes, in 0.1 M $HClO_4$ and at +1.20 V vs. SCE.

	IrO_2	**White-P25**	**Black-TiO_2-Oxy**
$R_s/\Omega\ cm^2$	2.97	4.96	4.94
$Q_f/\Omega^{-1}s^{n1}\ cm^{-2}$	0.38	0.35	0.17
n_1	0.78	1.09	1.10
$R_f/\Omega\ cm^2$	0.17	0.10	0.07
$Q_{dl}/\Omega^{-1}s^{n2}\ cm^{-2}$	0.42	0.26	0.39
n_2	0.87	0.93	0.87
$R_{ct}/\Omega\ cm^2$	1.30	0.93	0.97
$(C_{dl})_{Mansfeld}/F\ cm^{-2}$	0.37	0.23	0.34
$(C_{dl})_{Brug}/F\ cm^{-2}$	0.36	0.23	0.33
$R_{ct}C_{dl}/s$ *(Mansfeld)*	0.48	0.21	0.33
$R_{ct}C_{dl}/s$ *(Brug)*	0.47	0.21	0.32

Finally, to confirm the medium-term stability of this type of nano-composite catalyst, after their preliminary electrochemical testing, they were systematically investigated

through chronoamperometry experiments at constant potential, and indicative results are shown in Figure 11. It can be seen that catalyst performance retains ca 90% of its initial OER activity during a 7 h experiment.

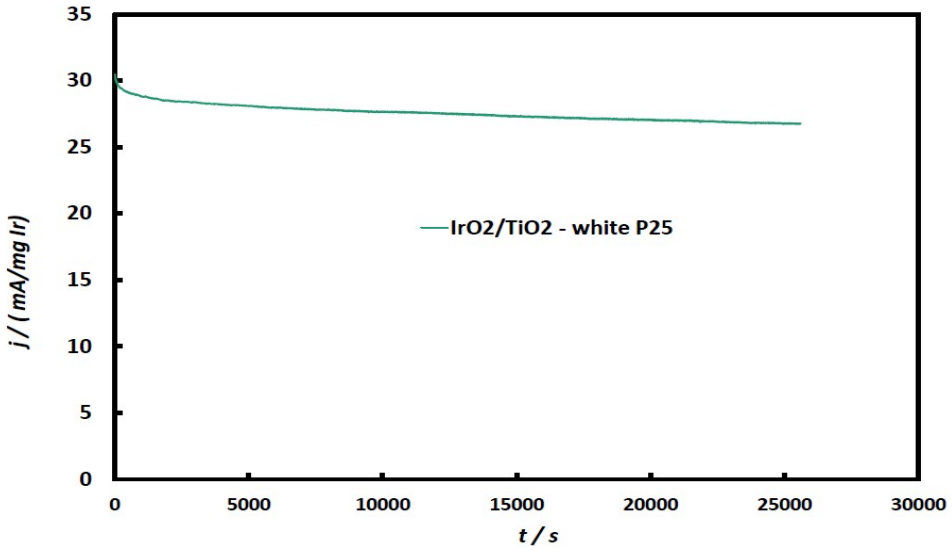

Figure 11. Chronoamperometric curves of the IrO_2/TiO_2 (white-P25) electrode, in a deaerated 0.1 M $HClO_4$ solution, at a constant potential of +1.3 V vs. SCE, for 7 h (not corrected for IR-drop).

3. Discussion

3.1. Analysis of Possible Photodeposition Routes and Mechanisms for Ir Deposition onto TiO_2 from Ir(III) Solutions

Being in an intermediate valence state between (0) and (IV), Ir(III) can either be photodeposited as metallic Ir or IrO_2. The first route involves the cathodic deposition of Ir at the Conduction Band (CB) of the illuminated TiO_2 semiconductor particles, whereby Ir(III) is photo-reduced to metallic Ir(0) by the photogenerated electrons at the Conduction Band (CB) (Figure 12a); this may be oxidized to IrO_2 during subsequent electrochemical potential cycling to sufficiently positive potential values (anodization) [28] or chemically oxidized by the $OH^{\cdot}$ radicals resulting from water photo-oxidation. In this case, the presence of methanol (in addition to water as a hole scavenger) should help the Ir(0) deposition process, minimizing electron–hole recombination. The second route (Figure 12b) involves the anodic deposition of IrO_2 at the valence band (VB), where Ir(III) is photo-oxidized to Ir(VI) by photogenerated holes (or $OH^{\cdot}$) and, in the presence of hydroxyl anions (either in the bulk of an alkaline solution or photo-produced at the CB of the illuminated semiconductor by water photo-reduction), can be chemically converted directly to IrO_2. In this case, methanol may limit IrO_2 deposition as it competes for the photogenerated holes (or $OH^{\cdot}$). Irrespective of the photodeposition route followed, and in accordance with the literature [23,27], the first step is reported to be the photo-assisted hydrolysis of the Ir(III) chloro-complex (Equations (1) and (2)):

$$IrCl_6^{-3}\ (UV) \rightarrow Ir^{3+}\ (aq) + 6\ Cl^- \quad (1)$$

$$\text{e.g., } IrCl_6^{-3} + 6OH^-\ (UV) \rightarrow Ir(OH)_6^{-3} + 6\ Cl^- \quad (2)$$

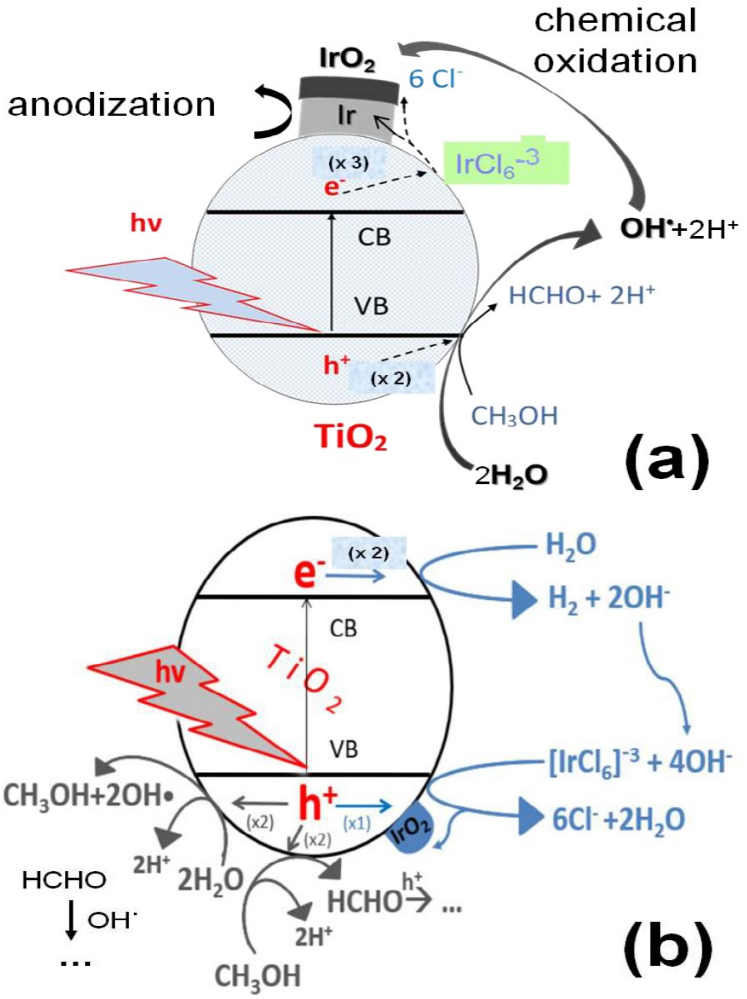

Figure 12. Photodeposition routes of Ir(III) on TiO_2; (**a**) cathodic deposition of Ir at CB and (**b**) anodic deposition of IrO_2 at VB. Methanol reactions at VB are also considered.

Predictions for the most favorable processes from a thermodynamic point of view can be made by studying the energy diagram (Figure 13) of TiO_2 (VB and CB energy levels for the given pH, deduced from data in [34,35]), as well as of the relevant red/ox couples (estimated from data in [36] to account for a pH of 11 and the Ir(III) concentration of 2×10^{-3} M). The higher the potential difference, $|\Delta E|$, between the energy levels of the TiO_2 photogenerated holes and electrons and that of a red/ox couple, the more likely the oxidation/reduction reaction, respectively. From the four possible reactions that the red/ox species shown in Figure 13 can undergo (two oxidations (red lines); two reductions (blue lines)), the oxidation of $Ir(III)_{aq}$ to IrO_2 ($|\Delta E| = 2.77$ V) is the most favorable, followed by its reduction to metallic Ir (($|\Delta E| = 2.01$ V):

$$Ir^{3+}\,(aq) + h^+ + 4OH^- \rightarrow IrO_2 + 2H_2O \quad (3)$$

$$\text{e.g., } Ir(OH)_6{}^{-3} + h^+ \rightarrow IrO_2 + 2H_2O + 2OH^- \quad (4)$$

or

$$Ir^{3+}\,(aq) + 3e^- \rightarrow Ir \quad (5)$$

$$\text{e.g., } Ir(OH)_6{}^{-3} + 3e^- \rightarrow IrO_2 + 6OH^- \quad (6)$$

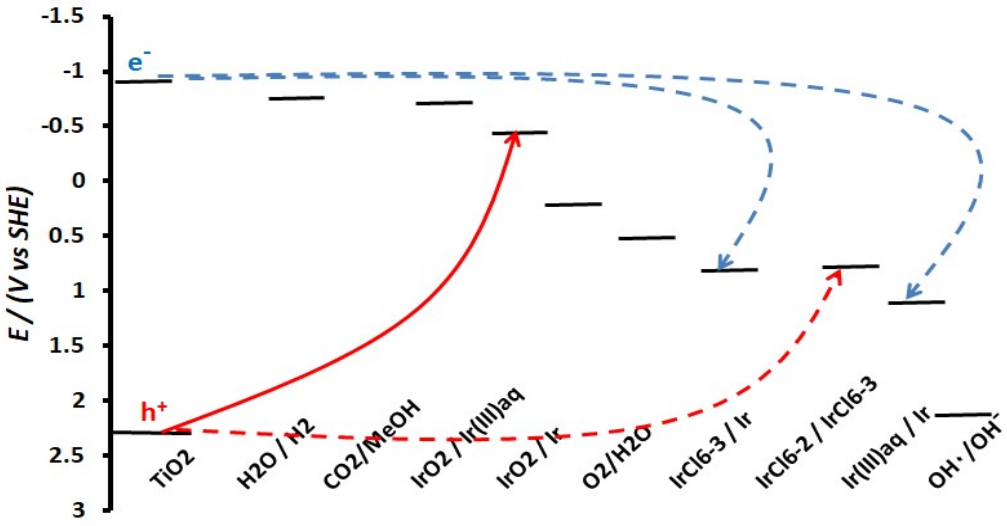

Figure 13. Energy diagram for TiO_2 (VB and CB) and various ox/red couples.

3.2. Evidence for the Photodeposition Mechanism and Form of Ir onto TiO_2 from Ir(III) Solutions

The interpretation of the spectroscopic and electrochemical results presented in the Results section above points to the photodeposition of Ir onto TiO_2 mainly as IrO_2, i.e., according to the reaction scheme of Figure 12 and reactions (3) and (4) above.

A first indication that this is the case is given by the effect of methanol addition on Ir content as measured by EDS: this falls from 26% *w*/*w* Ir in the absence of methanol to 19% and 2.5% *w*/*w* Ir upon addition of small quantities of methanol (0.15% and 1.5% *v*/*v* MeOH, respectively). As methanol is expected to compete with Ir(III) for the oxidizing photogenerated species (h^+ and/or $OH^{\cdot}$), it is expected to adversely affect Ir photodeposition, as has indeed been the case.

Second, the surface electrochemistry of Ir oxides and hydroxides depicted in the CV curves of Figures 7 and 8 shows a single redox peak in the case of catalysts prepared in the absence of methanol, at potentials where Ir(IV) oxide is known to be inter-converted to Ir(V) oxide, without the presence of additional Ir(III)/Ir(IV) redox peaks (as in the case of the commercial catalyst and catalysts prepared in the presence of methanol), whereby Ir(III) would originate from the electrochemical oxidation of metallic Ir to $Ir(OH)_3$ at lower applied potentials.

Finally, XPS confirmed that photodeposited Ir was mainly in its Ir(IV) oxidation state (with its percentage diminishing upon methanol addition).

3.3. Electrochemical Performance of the TiO_2-Supported IrO_2 towards OER

The surface electrochemistry of Ir oxides/hydroxides of the laboratory-prepared samples (depicted in the CV curves of Figure 7) allows for an estimate of the charge associated with the Ir(IV)/Ir(V) one-electron transformation (by integration of the single anodic peak/wave recorded in the 0.9–1.1 V potential range); this charge, q_{IrOx}, is in turn an indicator of the electrocatalyst electroactive surface area (esa). Both the esa and q_{IrOx} of IrO_x/TiO_2 catalysts are expected to depend on IrO_x quantity, specific surface area dispersion, and conductivity–IrO_x inter-connection, while their mass-specific variants (i.e., esa and q_{IrOx} per unit mass of IrO_x, esa and $q_{m,IrOx}$) should depend only on the latter two parameters. Table 3 below presents the values of mass-specific IrO_x-charge; in the case of the commercial, unsupported IrO_x catalyst (inset of Figure 7), since there are two couples of redox peaks/waves, corresponding to the 2e transformation of Ir(III) to Ir(V) via an In(IV) intermediate, half of the corresponding charge was used for comparison.

Table 3. Charge associated with 1e electrochemical oxidation of Ir in its surface oxides, as estimated from the anodic part of the CV curves of Figure 7.

	IrO_2/White-P25	IrO_2/Black-P25	IrO_2/White-Oxy	IrO_2/Black-Oxy	IrO_2
$q_{m,IrOx}$/mC mg_{Ir}^{-1}	85	54	94	125	199

It can be seen that the commercial catalyst has the highest mass-specific esa, despite the fact that, according to the TEM results of Figures 4 and 5, its aggregates are larger than the well-dispersed nanoparticles of the laboratory-made catalyst. This means that the decrease in conductivity/interparticle contact of the IrO_x/TiO_2 system (due to the semiconductor character of TiO_2) offsets their higher surface area.

Despite the apparent decrease in their esa, all of the prepared IrO_2/TiO_2 catalysts show better mass-specific electrocatalytic activity towards the OER than the commercial unsupported IrO_2 catalyst, as follows from the i_m vs. E curves of Figure 9a. In fact, the IrO_2/white-P25 and IrO_2/black-TiO_2-oxy catalysts show currents that are better than those of typical state-of-the-art catalysts reported in the literature; e.g., the ATO (antimony tin oxide)-supported $IrNiO_x$ catalysts of [37] exhibit a mass-specific current density of i_m = 90 mA/mg Ir at an overpotential of η = 280 mV, whereas our best catalysts provide the same currents at the lower overpotential of η = 240 mV. A more detailed comparison of the catalytic behavior of the materials reported in this work and some state-of-the-art catalysts in the literature is given in Table 4, which presents Ir mass-specific currents for OER at given overpotentials and was constructed by quoting or estimating values based on data reported in the referenced literature and in this work (corrected for IR-drop).

Table 4. Ir mass-specific currents for OER recorded at η = 260 mV and 280 mV, for OER from acid solutions, at supported IrO_2 nanoparticles.

Reference	Type of Catalyst	i_m/mAmg_{Ir}^{-1} (η = 260 mV)	i_m/mAmg_{Ir}^{-1} (η = 280 mV)
[38]	Ir nanodentrites/ATO	25	70
[37]	$IrNiO_x$/ATO	-	90
[39]	Ir/ATO-V	30	121
[40]	IrO_2/Nb-TiO_2	-	82
[14]	IrO_2-TiO_2	10	30
[20]	IrO_2-TiO_2 "blue"	-	100
This work	IrO_2/white-P25	271	877

The increased mass-specific activity of the prepared catalysts of this work with respect to the commercial catalyst (despite the latter having a larger apparent esa) is due to their higher intrinsic activity as highlighted by the curves of Figure 9b, where currents are normalized by the IrO_x charge (esa descriptor). The higher activity of IrO_2/TiO_2 with respect to the unsupported IrO_2 may be interpreted (in a way similar to the effect of Ni on IrO_2 [41]) by the difference in electronegativity and size of Ir and Ti, which may destabilize the Ir-OH bonds and increase the presence of activated O species that are intermediates in the OER mechanism. Also, Ir-O-Ir bonds may be disrupted by the formation of Ir-O-Ti bonds as suggested in [20] based on XPS data (in a way similar to the formation/partial decomposition of Ir-O-Ni bridges proposed in [42]). As suggested in [43], XPS analysis of the O 1s is crucial in determining the presence of oxygenated species that are key to OER at oxide electrodes; such measurements, carried out by our group on similar IrO_2/TiO_2 samples, have shown the existence of significant quantities of OH species on the surface of the catalyst [28].

4. Experimental Section

4.1. Synthesis of IrO_2 on Various TiO_2 Powders

Preparation of black-P25: Black-P25 was produced by ammonolysis. In a typical process, ~100 mg of commercially available white-P25 (Sigma-Aldrich Chemie GmbH, Taufkirchen, Germany) powder was loaded on a crucible and placed inside a quartz tube furnace. The tube ends were sealed, and the air inside was fully replaced by ammonia gas (NH_3 flushing). After sufficient flushing, the ammonia flow was significantly reduced and set at a constant flow rate. Then, the white-P25 was treated under ammonia at 100 °C, 300 °C, 500 °C, and 650 °C, staying at each temperature step for a total of 30 min (10 min reaching the set point temperature and 20 min for conditioning). After the last step at 650 °C, the TiO_2 P25® powder was treated there for 3 h and then freely cooled down to room temperature.

Preparation of TiO_2 from hydrated $TiOSO_4$ (white-TiO_2-oxy): Titanium (IV) oxysulfate hydrate ($TiOSO_4 \cdot xH_2O$) purchased from Sigma Aldrich, Taufkirchen, Germany, was used to prepare the *white-TiO_2-oxy* by a co-precipitation method. Titanium dioxide was precipitated at pH ~7 from an aqueous solution of $TiOSO_4$ titanium (IV) oxysulfate hydrate (0.1 M) by the addition of ammonia (VWR Chemicals, Lutterworth, UK). After aging overnight, the suspension was filtered with distilled water until it became sulfate- and ammonium ion-free and dried in air at 100 °C. The residue was crushed to a fine powder and calcined in a furnace at 700 °C for 3 h with a heating ramp rate of 5 °C min^{-1}.

Preparation of black TiO_2 black oxysulfate (black-TiO_2-oxy): The powder was produced by ammonolysis, as previously described.

Photodeposition of iridium nanoparticles on various TiO_2 supports: A photodeposition method was used for the preparation of supported OER catalysts. It is a simple and ambient temperature process, leading to the direct deposition of iridium dioxide onto the TiO_2 semiconducting powders by UV light irradiation, as described in our previous work [28]. An appropriate iridium salt aqueous solution of 120 mL (0.002 M K_3IrCl_6, Sigma-Aldrich Chemie GmbH, Taufkirchen, Germany), adjusted to pH = 11 (using 1 M KOH), was prepared and deaerated under N_2 purge for 15 min. The aqueous solution was transferred to a photochemical cylindrical reactor (250 cm^3), and TiO_2 powder (0.008 M) was also added. The UVA lamp (Radium Ralutec 9 W/78, λ = 350–400 nm, λ_{max} = 369 nm) was placed in a cylindrical quartz tube in the center of the photo-reactor. The materials were stirred for 20 min to prepare a homogeneous slurry. The latter was kept under UV light irradiation for 8 h to achieve (in most cases) ca 25 wt% of Ir photodeposited on the TiO_2 nanoparticle substrate. Vacuum filtration followed with distilled water, and the resulting powder catalyst (gray, blue–black, or black in color, depending on the TiO_2 support) was dried overnight at room temperature. The resulting solid was ground to a fine powder using an agate mortar. The four types of prepared samples were (a) IrO_2/TiO_2 (white-P25), (b) IrO_2/TiO_2 (black-P25), (c) IrO_2/TiO_2 (white-TiO_2-oxy), and (d) IrO_2/TiO_2 (black-TiO_2-oxy).

4.2. Structural, Chemical, and Morphological Measurements

The lattice parameters and the crystalline phases of the prepared TiO_2 substrates were characterized by an X-ray Diffractometer (XRD) (Brucker AXS D8, Karlsruhe, Germany) equipped with a nickel foil monochromator (40 kV, 20 mA) at scattering angles 2θ between 10 and 80° (0.05° s^{-1} scan rate) using Cu Ka_1 radiation. The diffraction pattern was analyzed by the Scherrer equation giving the crystallite size of each synthesized powder. The surface morphology and elemental composition were analyzed using a Field Emission Scanning Electron Microscope (FESEM; 7000 JEOL, Tokyo, Japan) with energy-dispersive X-ray spectroscopy, operating at 20 keV. Diffuse *reflectance (DR)* UV–visible spectra were measured by a Perkin Elmer Lambda 950 UV/Vis/NIR spectrophotometer working at λ = 250–2500 nm, and it was employed to measure the absorption/reflection spectrums. The optical energy bandgaps were extracted by the Tauc plot of Equation (7).

$$(ahv)^n = hv - E_g \quad (7)$$

where α is the absorption coefficient, h is the Planck constant, ν is the radiation frequency, and n is 0.5 or 2 for indirect or direct transition. The energy gap was also calculated at the interception of the linear fit of the appropriate region on the Tauc plot (where α is zero). X-ray photoelectron spectroscopy (XPS) measurements were performed using a Kratos Axis Ultra DLS spectrometer, Manchester, UK, equipped with a non-monochromatic Al X-ray source (under vacuum better than 10^{-8} Pa at a 90° take-off angle). The Ir4f line was subjected to an additional fitting procedure with XPSPEK4.1 software to determine the chemical oxidation states in the absence and presence of methanol. Transmission Electron Microscopy (TEM) images were obtained for the photocatalytically prepared powders on a JEM 2100 (JEOL, Tokyo, Japan) equipped with a LaB_6 filament at an accelerating voltage of 200 kV.

4.3. Electrochemical Measurements

Procedure: The surface electrochemistry and the electrochemical oxygen evolution activity and stability of the synthesized catalysts were studied using a PGSTAT302N potentiostat (Metrohm Autolab, Herisau, Switzerland), in a standard three-compartment glass cell equipped with a Luggin capillary and comprising a Pt foil counter electrode, a saturated calomel electrode reference electrode, and a glassy carbon (GC) working electrode substrate-current collector (3 mm diameter). The experiments were recorded in a 0.1 M $HClO_4$ (70%, Sigma-Aldrich, Chemie GmbH, Taufkirchen, Germany) electrolyte at 25 °C. The system was purged with N_2 for 15 min before the working electrode was placed in the electrolyte to remove dissolved oxygen before the electrochemical measurements were recorded.

Electrode preparation: Prior to every measurement, the glassy carbon (GC) working electrode was polished with an alumina slurry, and then it was sonicated to remove impurities and any residual polishing slurry. Catalyst inks were coated as a thin-film layer on the GC surface of a Rotating Disk Electrode (RDE) with the resulting loading of Ir in the 0.5–1.0 mg cm^{-2} range. The ink suspension was composed of x mg catalyst (according to the w/w % Ir composition from EDS), 6% w/w Nafion® perfluorinated resin solution (5 wt% Sigma-Aldrich) and ethanol as the ionic binder and solvent, respectively. It was mixed and ultrasonically homogenized for 30 min. The temperature of the sonication was kept at ca 35 °C to avoid evaporation of the solvent.

Electrochemical characterization: The surface electrochemistry of IrO_2/TiO_2 was studied by cyclic voltammetry (CV) experiments in the potential range between −0.3 and 1.1 V vs. SCE at 25 mV s^{-1} until a stable CV was obtained. The last stable cycle was used to estimate the IrO_x charge. The OER polarization curves were recorded by Linear Sweep Voltammetry (LSV) at 1600 rpm and a slow scan rate (5 mV s^{-1}). Electrochemical Impedance Spectroscopy (EIS) measurements were carried out in the frequency range of 100 kHz to 100 mHz with an amplitude of 10 mV. The ohmic resistance was estimated from the EIS measurements and use for IR compensation of the LSV curves. For the medium-term stability tests, the electrode was held at a constant potential of 1.3 V vs. SCE under a rotation speed of 1600 rpm.

5. Conclusions

Summarizing, this study has demonstrated the following:

a. We showed the successful UV light photodeposition of iridium from $IrCl_6^{-3}$ solutions onto TiO_2 powders in the form of IrO_x nanoparticles. This comprises an ambient temperature and simple chemistry alternative for the preparation of IrO_2-TiO_2 composites (advantages characteristic of photocatalytic synthetic methods when compared to other techniques for electrocatalyst preparation such as hydrothermal or/and sonochemical techniques; see, for example, [44,45]).
b. All of the thus prepared IrO_x/TiO_2 catalysts (despite a moderate apparent electroactive surface area due to electronic conductivity losses) exhibited superior mass-specific

activity for OER to that of the commercial unsupported IrO_2 catalyst, as a result of increased intrinsic activity, due to Ir-Ti interactions.

c. The best of the prepared catalysts (IrO_2/TiO_2 (white-P25), 26% *w*/*w* Ir, and IrO_2/TiO_2 (black-oxy), 28% *w*/*w* Ir), exhibited mass-specific OER activities higher than that of state-of-the-art supported IrO_x powder catalysts (it can be estimated as high as 100 mA mg^{-1} Ir at η = 243 mV).

d. The fact that the IrO_x/TiO_2 catalysts of this work outperformed IrO_x catalysts supported on conducting substrates (such as doped TiO_2 and antimony-doped SnO_2 (ATO)) indicates that the well-dispersed IrO_x particles anchored on TiO_2 by the proposed photodeposition method can provide sufficient conductivity to the composite material.

Author Contributions: Conceptualization, S.S. and J.G.; methodology, A.B., J.G. and V.B.; validation, A.B.; formal analysis, A.B.; investigation, A.B., C.Z., M.C., O.-N.S. and E.M.; writing—original draft preparation, A.B.; writing—review and editing, V.B. and S.S.; visualization, A.B. and S.S.; supervision, S.S. All authors have read and agreed to the published version of the manuscript.

Funding: This research project is implemented in the framework of H.F.R.I call "Basic research Financing (Horizontal support of all Sciences)" under the National Recovery and Resilience Plan "Greece 2.0" funded by the European Union—NextGenerationEU (H.F.R.I. Project Number: 16443; Project Acronym: CATSOLHYDROGEN).

Institutional Review Board Statement: Not applicable.

Informed Consent Statement: Not applicable.

Data Availability Statement: The original contributions presented in this study are included in the article; further inquiries can be directed to the corresponding author.

Acknowledgments: The bilateral joint research project "Modified nanomaterials for electro- and photoelectrocatalytic applications—synthesis and characterization" 2022–2025 between the Bulgarian Academy of Sciences (BAS) and the Aristotle University of Thessaloniki, Greece, is gratefully acknowledged. S.Armyanov and E.Valova (BAS) are acknowledged for XPS data and analysis.

Conflicts of Interest: The authors declare no conflicts of interest.

References

1. Guan, D.; Wang, B.; Zhang, J.; Shi, R.; Jiao, K.; Li, L.; Wang, Y.; Xie, B.; Zhang, Q.; Yu, J.; et al. Hydrogen society: From present to future. *Energy Environ. Sci.* **2023**, *16*, 4926–4943. [CrossRef]
2. Lin, X.; Seow, J.Z.Y.; Xu, Z.J. A brief introduction of electrode fabrication for proton exchange membrane water electrolyzers. *J. Phys. Energy* **2023**, *5*, 034003. [CrossRef]
3. Wu, Q.; Wang, Y.; Zhang, K.; Xie, Z.; Sun, K.; An, W.; Liang, X.; Zou, X. Advances and status of anode catalysts for proton exchange membrane water electrolysis technology. *Mater. Chem. Front.* **2023**, *7*, 1025–1045. [CrossRef]
4. Liu, Y.; Liang, X.; Chen, H.; Gao, R.; Shi, L.; Yang, L.; Zou, X. Iridium-containing water-oxidation catalysts in acidic electrolyte. *Chin. J. Catal.* **2021**, *42*, 1054–1077. [CrossRef]
5. Moriau, L.; Smiljanić, M.; Lončar, A.; Hodnik, N. Supported Iridium-based Oxygen Evolution Reaction Electrocatalysts-Recent Developments. *ChemCatChem* **2022**, *14*, e202200586. [CrossRef] [PubMed]
6. Bagheri, S.; Muhd Julkapli, N.; Bee Abd Hamid, S. Titanium dioxide as a catalyst support in heterogeneous catalysis. *Sci. World J.* **2014**, *2014*, 727496. [CrossRef] [PubMed]
7. Lavacchi, A.; Bellini, M.; Berretti, E.; Chen, Y.; Marchionni, A.; Miller, H.A.; Vizza, F. Titanium dioxide nanomaterials in electrocatalysis for energy. *Curr. Opin. Electrochem.* **2021**, *28*, 100720. [CrossRef]
8. Bernt, M.; Siebel, A.; Gasteiger, H.A. Analysis of voltage losses in PEM water electrolyzers with low platinum group metal loadings. *J. Electrochem. Soc.* **2018**, *165*, F305–F314. [CrossRef]
9. Bernt, M.; Schramm, C.; Schröter, J.; Gebauer, C.; Byrknes, J.; Eickes, C.; Gasteiger, H.A. Effect of the IrO_x conductivity on the anode electrode/porous transport layer interfacial resistance in PEM water electrolyzers. *J. Electrochem. Soc.* **2021**, *168*, 084513. [CrossRef]
10. Böhm, D.; Beetz, M.; Gebauer, C.; Bernt, M.; Schröter, J.; Kornherr, M.; Zoller, F.; Bein, T.; Fattakhova-Rohlfing, D. Highly conductive titania supported iridium oxide nanoparticles with low overall iridium density as OER catalyst for large-scale PEM electrolysis. *Appl. Mater. Today* **2021**, *24*, 101134. [CrossRef]

11. Bernsmeier, D.; Bernicke, M.; Schmack, R.; Sachse, R.; Paul, B.; Bergmann, A.; Strasser, P.; Ortel, E.; Kraehnert, R. Oxygen Evolution Catalysts Based on Ir–Ti Mixed Oxides with Templated Mesopore Structure: Impact of Ir on Activity and Conductivity. *ChemSusChem* **2018**, *11*, 2367–2374. [CrossRef] [PubMed]
12. Mazúr, P.; Polonský, J.; Paidar, M.; Bouzek, K. Non-conductive TiO_2 as the anode catalyst support for PEM water electrolysis. *Int. J. Hydrogen Energy* **2021**, *37*, 12081–12088. [CrossRef]
13. Lee, Y.; Scheurer, C.; Reuter, K. Epitaxial Core-Shell Oxide Nanoparticles: First-Principles Evidence for Increased Activity and Stability of Rutile Catalysts for Acidic Oxygen Evolution. *ChemSusChem* **2022**, *15*, e202200015. [CrossRef] [PubMed]
14. Oakton, E.; Lebedev, D.; Povia, M.; Abbott, F.D.; Fabbri, E.; Fedorov, A.; Nachtegaal, M.; Copéret, C.; Schmidt, T.J. IrO_2-TiO_2: A High-Surface-Area, Active, and Stable Electrocatalyst for the Oxygen Evolution Reaction. *ACS Catal.* **2017**, *7*, 2346–2352. [CrossRef]
15. Kim, M.Y.; Ban, H.J.; Song, Y.-W.; Lim, J.; Park, S.-J.; Kim, W.-J.; Hong, Y.; Kang, B.S.; Kim, H.-S. Synthesis and electrochemical properties of nanocomposite IrO_2/TiO_2 anode catalyst for SPE electrolysis cell. *Int. J. Hydrogen Energy* **2022**, *47*, 31098–311108. [CrossRef]
16. Phama, C.V.; Bühlera, M.; Knöppel, J.; Bierling, M.; Seeberger, D.; Escalera-López, D.; Mayrhofer, K.J.J.; Cherevko, S.; Thiele, S. IrO_2 coated TiO_2 core-shell microparticles advance performance of low loading proton exchange membrane water electrolyzers. *Appl. Catal. B Environ.* **2020**, *269*, 118. [CrossRef]
17. Ying, Y.; Salomon, J.F.G.; Lartundo-Rojas, L.; Moreno, A.; Meyer, R.; Damin, C.A.; Rhodes, C.P. Hydrous cobalt–iridium oxide two-dimensional nanoframes: Insights into activity and stability of bimetallic acidic oxygen evolution electrocatalysts. *Nanoscale Adv.* **2021**, *3*, 1976–1996. [CrossRef] [PubMed]
18. Moriau, L.; Bele, M.; Marinko, Z.; Ruiz-Zepeda, F.; Podboršek, G.K.; Šala, M.; Šurca, A.K.; Kovač, J.; Arčon, I.; Jovanovič, P.; et al. Effect of the Morphology of the High-Surface-Area Support on the Performance of the Oxygen-Evolution Reaction for Iridium Nanoparticles. *ACS Catal.* **2021**, *11*, 670–681. [CrossRef] [PubMed]
19. Liu, G.; Hou, F.; Wang, X.; Fang, B. Ir-IrO_2 with heterogeneous interfaces and oxygen vacancies-rich surfaces for highly efficient oxygen evolution reaction. *Appl. Surf. Sci.* **2023**, *615*, 156333. [CrossRef]
20. Nguyen, C.T.K.; Tran, N.Q.; Le, T.A.; Lee, H.-L. Covalently Bonded Ir(IV) on Conducted Blue TiO_2 for Efficient Electrocatalytic Oxygen Evolution Reaction in Acid Media. *Catalysts* **2021**, *11*, 1176. [CrossRef]
21. Yin, J.; Jin, J.; Lu, M.; Huang, B.; Zhang, H.; Peng, Y.; Xi, P.; Yan, C.-H. Iridium Single Atoms Coupling with Oxygen Vacancies Boosts Oxygen Evolution Reaction in Acid Media. *J. Am. Chem. Soc.* **2020**, *142*, 18378–18386. [CrossRef] [PubMed]
22. Lu, Z.-X.; Shi, Y.; Yan, C.-F.; Guo, C.-Q.; Wang, Z.-D. Investigation on IrO_2 supported on hydrogenated TiO_2 nanotube array as OER electro-catalyst for water electrolysis. *Int. J. Hydrogen Energy* **2017**, *42*, 3572–3578. [CrossRef]
23. Jang, H.; Lee, J. Iridium oxide fabrication and application: A review. *J. Energy Chem.* **2020**, *46*, 152–172. [CrossRef]
24. Li, P.; Kong, L.; Liu, J.; Yan, L.; Liu, S. Photoassisted Hydrothermal Synthesis of IrO_x-TiO_2 for Enhanced Water Oxidation. *ACS Sust. Chem. Eng.* **2019**, *7*, 17941–17949. [CrossRef]
25. Iwase, A.; Kato, H.; Kudo, A. A Novel Photodeposition Method in the Presence of Nitrate Ions for Loading of an Iridium Oxide Cocatalyst for Water Splitting. *Chem. Lett.* **2005**, *34*, 946–947. [CrossRef]
26. Bledowski, M.; Wang, L.; Neubert, S.; Mitoraj, D.; Beranek, R. Improving the Performance of Hybrid Photoanodes for Water Splitting by Photodeposition of Iridium Oxide Nanoparticles. *J. Phys. Chem. C* **2014**, *118*, 18951–18961. [CrossRef]
27. Wu, Q.; Xu, D.; Xue, N.; Liu, T.; Xiang, M.; Diao, P. Photo-catalyzed surface hydrolysis of iridium(III) ions on semiconductors: A facile method for the preparation of semiconductor/IrO_x composite photoanodes toward oxygen evolution reaction. *Phys. Chem. Chem. Phys.* **2017**, *19*, 145–154. [CrossRef] [PubMed]
28. Dimitrova, N.; Banti, A.; Spyridou, O.-N.; Papaderakis, P.; Georgieva, G.; Sotiropoulos, S.; Valova, E.; Armyanov, S.; Tatchev, D.; Hubin, A.; et al. Photodeposited IrO_2 on TiO_2 support as a catalyst for oxygen evolution reaction. *J. Electroanal. Chem.* **2021**, *900*, 115720. [CrossRef]
29. Ouattara, L.; Fierro, S.; Frey, O.; Koudelka, M.; Comninellis, C. Electrochemical comparison of IrO_2 prepared by anodic oxidation of pure iridium and IrO_2 prepared by thermal decomposition of H_2IrCl_6 precursor solution. *J. Appl. Electrochem.* **2009**, *39*, 1361–1367. [CrossRef]
30. Nga Ngo, T.H.; Love, J.; O'Mullane, A.P. Investigating the Influence of Amorphous/Crystalline Interfaces on the Stability of IrO_2 for the Oxygen Evolution Reaction in Acidic Electrolyte. *ChemElectroChem* **2023**, *10*, e202300438. [CrossRef]
31. Hsu, C.H.; Mansfeld, F. Technical note: Concerning the conversion of the constant phase element parameter Y0 into a capacitance. *Corrosion* **2001**, *57*, 747–748. [CrossRef]
32. Brug, G.J.; van den Eeden, A.L.G.; Sluyters-Rehbach, M.; Sluyters, J.H. The analysis of electrode impedances complicated by the presence of a constant phase element. *J. Electroanal. Chem.* **1984**, *176*, 275–295. [CrossRef]
33. Papaderakis, A.; Tsiplakides, D.; Balomenou, S.; Sotiropoulos, S. Electrochemical impedance studies of IrO_2 catalysts for oxygen evolution. *J. Electroanal. Chem.* **2015**, *757*, 216–224. [CrossRef]
34. Yong, X.; Schoonen, M.A.A. The absolute energy positions of conduction and valence bands of selected semiconducting minerals. *Am. Mineral.* **2000**, *85*, 543–556. [CrossRef]
35. Hien, T.T.; Quang, N.D.; Kim, C.; Kim, D. Energy diagram analysis of photoelectrochemical water splitting process. *Nano Energy* **2019**, *57*, 660–669. [CrossRef]
36. Bard, A.J.; Parsons, R.; Jordan, J. *Standard Potentials in Aqueous Solution*; M. Dekker: New York, NY, USA, 1985; pp. 385–834.

37. Nong, H.N.; Oh, H.S.; Reier, T.; Willinger, E.; Willinger, M.G.; Petkov, V.; Teschner, D.; Strasser, P. Oxide-supported IrNiOx core-shell particles as efficient, cost-effective, and stable catalysts for electrochemical water splitting. *Angew. Chem. Int. Ed.* **2015**, *54*, 2975–2979. [CrossRef] [PubMed]
38. Oh, H.-S.; Nong, H.N.; Reier, T.; Gliech, M.; Strasser, P. Oxide-supported Ir nanodendrites with high activity and durability for the oxygen evolution reaction in acid PEM water electrolyzers. *Chem. Sci.* **2015**, *6*, 3321–3328. [CrossRef] [PubMed]
39. Wang, L.; Song, F.; Ozouf, G.; Geiger, D.; Morawietz, T.; Handl, M.; Gazdzicki, P.; Beauger, C.; Kaiser, U.; Hiesgen, R.; et al. Improving the activity and stability of Ir catalysts for PEM electrolyzer anodes by SnO_2:Sb aerogel supports: Does V addition play an active role in electrocatalysis? *J. Mater. Chem. A* **2017**, *5*, 3172–3178. [CrossRef]
40. Hu, W.; Chen, S.; Xia, Q. IrO_2/Nb-TiO_2 electrocatalyst for oxygen evolution reaction in acidic medium. *Int. J. Hydrogen Energy* **2014**, *39*, 6967–6976. [CrossRef]
41. Papaderakis, A.; Pliatsikas, N.; Prochaska, C.; Vourlias, G.; Patsalas, P.; Tsiplakides, D.; Balomenou, S.; Sotiropoulos, S. Oxygen Evolution at IrO_2 Shell–Ir−Ni Core Electrodes Prepared by Galvanic Replacement. *J. Phys. Chem. C* **2016**, *120*, 19995–20005. [CrossRef]
42. Reier, T.; Pawolek, Z.; Cherevko, S.; Bruns, M.; Jones, T.; Teschner, D.; Selve, S.; Bergmann, A.; Nong, H.N.; Schlögl, R.; et al. Molecular insight in structure and activity of highly efficient, low-Ir Ir-Ni oxide catalysts for electrochemical water splitting (OER). *J. Am. Chem. Soc.* **2015**, *137*, 13031–13040. [CrossRef] [PubMed]
43. Zhang, H.; Guan, D.; Gu, Y.; Xu, H.; Wang, C.; Shao, Z.; Guo, Y. Tuning synergy between nickel and iron in Ruddlesden–Popper perovskites through controllable crystal dimensionalities towards enhanced oxygen-evolving activity and stability. *Carbon Energy* **2024**, e465. [CrossRef]
44. Yadav, A.A.; Hunge, Y.M.; Kang, S.-W. Highly efficient porous morphology of cobalt molybdenum sulfide for overall water splitting reaction. *Surf. Interfaces* **2021**, *23*, 101020. [CrossRef]
45. Yadav, A.A.; Hunge, Y.M.; Kang, S.-W. Ultrasound assisted synthesis of highly active nanoflower-like CoMoS4 electrocatalyst for oxygen and hydrogen evolution reactions. *Ultrason. Sonochem.* **2021**, *72*, 105454. [PubMed]

Disclaimer/Publisher's Note: The statements, opinions and data contained in all publications are solely those of the individual author(s) and contributor(s) and not of MDPI and/or the editor(s). MDPI and/or the editor(s) disclaim responsibility for any injury to people or property resulting from any ideas, methods, instructions or products referred to in the content.